Northumbria Research Link

Northumbria University NEWCASTLE

University Library

Shape evolution of droplets growing on linear micro–grooves

Ciro Semprebon,[†,‡] Carsten Herrmann,[¶] Bang-Yan Liu,[¶] Ralf Seemann,[¶,†] and Martin Brinkmann[*,¶,§]

†Max-Planck Institute for Dynamics and Self-Organization, 37077 Göttingen, Germany
‡Smart Materials and Surfaces Laboratory, Department of Physics and Electrical Engineering, Northumbria University, UK
¶Experimental Physics, Saarland University, 66123 Saarbrücken, Germany
§Max-Planck Institute for Dynamics and Self–Organization, 37077 Göttingen, Germany

E-mail: martin.brinkmann@physik.uni-saarland.de

Abstract

Anisotropic spreading of liquids and elongated droplet shapes are often encountered on surfaces decorated with a periodic micro–pattern of linear surface topographies. Numerical calculations and wetting experiments show that the shape evolution of droplets that are slowly growing on a surface with parallel grooves can be grouped into two distinct morphological regimes. In the first regime, the liquid of the growing droplet spreads only into the direction parallel to the grooves. In the second regime, the three phase contact line advances also perpendicular to the grooves while the growing droplets approach a scale–invariant shape. Here, we demonstrate that shapes of droplets in contact to a large number of linear grooves are identical to the shapes of droplets confined to a plane chemical stripe, where this mapping of shapes is solely based on the knowledge of the cross–section of the linear grooves and the material contact angle. The spectrum of interfacial shapes on the chemical stripe can be exploited to predict the particular growth mode and the asymptotic value of the base eccentricity in the limit of droplets covering a large number of grooves. The proposed model shows an excellent agreement with experimentally observed base eccentricities for droplets on grooves of various cross–section. The universality of the model is underlined by the accurate match with available literature data for droplets eccentricities on parallel chemical stripes.

1 Introduction

Surface micro–structures can enhance or inhibit spreading of a liquid into certain directions,[1] giving rise to anisotropic droplet shapes[2] and interfacial instabilities.[3] Patterns of linear micro–structures that are able to guide the motion of water droplets have been discovered on the surfaces of many plants and animals, for examples on daisy florets,[4] or the wings of butterflies.[5] The development of anisotropic surface features appears to be an evolutionary advantage achieved by living organisms, allowing a more efficient collection, control or disposal of liquids. Inspired by the rich spectrum of natural microstructures, studies of anisotropic spreading of liquids have been conducted also for a large number of artificial patterns of linear topographic[6–15] and chemical[16–18] surface features. To date, various techniques are available to fabricate artificial microstructures that mimic the wetting properties of their natural counterparts. Periodic arrays of linear micro–structures with the abil-

ity to direct liquid motion can be obtained by interference lithography,[9] controlled wrinkling of silicone rubber,[8] chemical vapor deposition through masks,[17] or by anisotropic wet etching silicon wafers. Typical features of both natural and synthetic surface patterns are much smaller than a millimeter down to the sub–micron range.[9]

The wettability of an ideally smooth and chemically homogeneous solid surface by a liquid is commonly expressed in terms of Young's angle θ_0 which is determined by the surface energies of the interfaces. In the presence of surface defects advancing and receding motion occur at different angles, defining the range of contact angle hysteresis.[19] On a randomly rough surface, the macroscopic advancing and receding contact angles do not depend on the orientation of the interface. The wetting properties of linear micro–topographies, however, are characterized by two specific contact angles that depend on the material and the geometry of the grooves: The de–pinning angle θ_a, on the one hand, represents the largest apparent contact angle at which the contact line is still pinned in a direction orthogonal to the grooves. At sharp edges the contact line is immobilised if the contact angle falls into a certain range (canthotaxis).[6,20–22] On smooth topographies, however, the contact line is allowed to continuously shift while approaching the region where the slope of the topography is maximum. The Wenzel angle θ_w of the periodic topography, on the other hand, is the apparent contact angle in a thermodynamic state of minimum interfacial energy and relates to the effective surface energy of the corrugated surface, regardless any detail of the topography, as long as it is linear.

In the present work we show that the magnitude of the interfacial pinning force created by linear grooves and the overall wettability of the surface, here expressed in terms of the de–pinning angle and the Wenzel angle of the pattern, respectively, control the shape evolution of liquid droplets during a slow volume increase. Two qualitatively different morphological growth modes are observed in numerical calculations and in experiments, c.f. Fig. 1 (a–c): For sufficiently strong pinning forces (i.e.

sufficiently large pinning angles compared to Wenzel angles), large portions of the lateral droplet interface are immobilized by the ridges causing the droplet to grow exclusively into the direction of the grooves. In the opposite case of weak pinning forces, however, the lateral segments of the droplet interface are able to traverse the grooves which gives rise to an oscillatory growth into both surface directions. In contrast to droplets undergoing unidirectional growth, droplets in this bidirectional growth regime approach an anisotropic, but scale–invariant shape.

The appearance of different growth modes is not fully controlled by the de–pining angle and Wenzel angle, although both quantities are uniquely determined by the material contact angle and the cross–section of the grooves. Examples from our numerical energy minimizations shown in Fig. 1(a,b) and wetting experiments shown in Fig. 1(c) demonstrates that it is possible to encounter both lateral and unidirectional growth modes on the same sample. We will show rigorously that the crucial condition is the number of grooves occupied by the first drop after deposition. The emergence of different morphologies of droplets growing on linear groove pattern is closely related to the mechanical bistability between elongated and a localized liquid shapes on the plane chemical stripe.[23,24] Although the possibility to find different droplet morphologies on substrates with micro–grooves has been already mentioned in Refs.,[6,9,25] the implications of the morphological bistability on the shape evolution of slowly growing droplets has been largely overlooked.

In this work, to explain the origin of the two distinct growth modes, we first show that the shapes of droplets wetting a large number of grooves can be matched to certain shapes of droplets on a plane chemical stripe that is surrounded by a fully non-wetting surface. This opens the possibility to determine the lateral contact angle of the pinned droplet as a function of the degree of confinement. By virtue of this universal relation, we are able to predict not only the growth modes for a given de–pinning angle θ_a and Wenzel angle θ_w, but also to accurately quantify the shape of a droplet that cov-
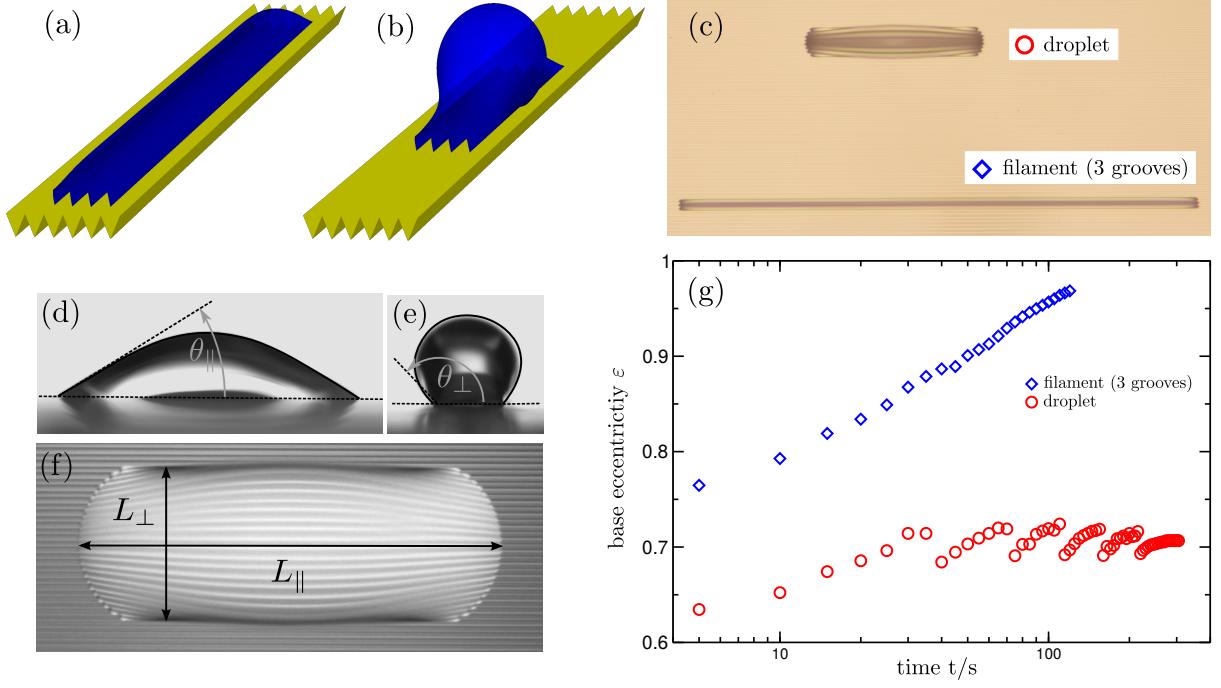
Figure 1: (a) and (b): Shapes of liquid droplets in contact to v–grooves with a slope angle $\psi = 65°$ and advancing contact angle $\theta_0 = 70°$ (Wenzel angle $\theta_w = 36°$). (c): Water morphologies on a periodic v-groove micro-pattern made of NOA84 surface with $\psi = 54.7°$ and $\theta_0 = (70 \pm 4)°$. (d-f): Optical micrographs of a growing water droplet on a Si–wafer with v–grooves in side view perpendicular to groove direction, (d), head–on view into groove direction, (e), and in top view, (f). Note that the interfacial contour of the liquid morphology in (e) is not a circular arc and has been fitted by a cubic spline. (g): Temporal evolution of the base eccentricity ϵ of the two condensing water morphologies shown in panel (c), c.f. also the definition of ε Eqn. (1).

3

ers an asymptotically large number of grooves. Our results can be directly applied to predict the anisotropic shapes of drops on any type of linear patterns, and help designing the surface topographies and chemical patterns to achieve elongated drops of any prescribed shape.

Our article is organized as follows: A short outline of the set–up used in the wetting experiments and the numerical model is given in Sec. 2. The shape evolution of slowly growing droplets observed in our experiments are discussed in Sec. 3. Criteria for the mechanical stability of asymptotically long droplets growing into the direction of the grooves are presented in Sec. 4, while the mapping to shapes confined to a plane chemical stripe is introduced and explained in Sec. 5. In the following Sec. 6, we compare the predictions of plane stripe model with numerical and experimental results for particular linear topographic or chemical patterns. Predictions for the base eccentricity are also compared to an existing model in Sec. 7. A concluding evaluation of the presented findings and an outlook on possible applications is given in Sec. 9.

2 Methods

Protocols of the wetting experiments and the extraction of relevant experimental data will be outlined in Sec. 2.1. Details of the finite element representation of the liquid–vapor interface of the droplets and the numerical minimization of the interfacial energy are outlined Sec. 2.2.

2.1 Wetting experiments

Substrates with periodic patterns of linear grooves of various homogeneous cross–section are obtained by soft lithography applying a double molding process, c.f. also Fig. 2. Primary masters for u–shaped grooves with a typical periodicity of $10 \mu m$ are fabricated using holographic LASER ablation from an imide substrate. Masters with rectangular grooves are obtained by standard photolithography in SU-8 (Microchem) while masters with v–shaped grooves are fabricated in silicon by standard
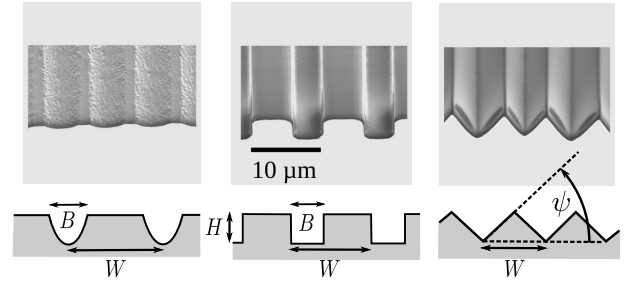

Figure 2: Scanning electron micrographs of linear grooves with u-shaped rectangular, and v–shaped cross–section, respectively, used in our experiments. Definitions of groove depth H and groove width B, as well as the period W and slope angle ψ are indicated.

photolithography and subsequent anisotropic wet etching (Zentrum für Mikrotechnologien Chemnitz, Germany). In a first molding step a negative polydimethylsiloxan rubber (Sylgard 184, Dow Corning) replica is cast from such a primary master. In a second molding step the final samples are cast from the Sylgard replica using UV curable glues from the NOA 61, 81, 85 (Norland Optical Adhesives). The topography of the solidified UV glue samples are characterized by Scanning Force Microscopy in Tapping Mode™ (Bruker Icon, FastScan) and Scanning Electron Microscopy (SEM). Aging of the samples under ambient conditions, plasma treatment (Diener electric, Femto) or gas phase silanization of perfluorodecyltrichlorosilane (ABCR 111155) is employed to obtain advancing and receding material contact angles for water in the range $41° \leq \theta_0 \leq 122°$ on the respective surfaces.

Small water droplets are grown on structured substrate by vapor condensation from the gas phase on hygroscopic chemicals seeds, such as calcium chloride (VWR Prolabo) or glycerol (99 %, Grüssing). To control the condensation rate of water, the sample is cooled below room temperature using a Peltier element. Larger droplets are grown by dispensing ultra-pure water (Thermo Scientific TKA-GenPure) from below through a $100 \mu m$ diameter hole drilled in the sample that is connected by Teflon tubings to a syringe pump. Typical droplet growth times are about $10 \, min$ in both protocols. The

typical velocity of the contact line during the continuous growth is $10\mu m/s$ giving a capillary number of order $Ca \approx 10^{-8}$. Under these conditions viscous stresses at the contact lines are negligible[26] and we can assume mechanically equilibrated static interfacial configurations. Faster motion is temporarily observed after spilling, as the pair of kinks created quickly propagates. Such motion terminates once the newly filled grooves closes up with the drop length, and after which the slow growth continues.

Interfacial profiles are imaged from two perpendicular directions at a rate of one frame per second employing a modified contact angle measurement device (OCA 20, Data Physics) and a Leica Macroscope Z16 mounted in upright geometry. Figure 1(c–f) shows examples of a water droplets emerging during condensation on a substrate decorated with linear grooves of v–shaped cross–section. Typical images in top and side view are shown in Fig. 1(d,e). Shapes of the growing droplets are quantified by the parallel and perpendicular base extensions $L_\parallel$ and $L_\perp$, respectively, with respect to the direction of the linear pattern, c.f. the snapshots of a typical droplet in our condensation experiments shown in Fig. 1(f). In addition, we extract the apparent contact angles $\theta_\parallel$ and $\theta_\perp$ from the images of the droplet contour in side and head-on view, respectively, as shown in Fig. 1(d) and (e).

2.2 Numerical energy minimizations

The morphological evolution of slowly growing droplets in contact to a linear surface pattern can be described, in a good approximation, as a sequence of mechanical equilibrium conformations of the liquid interface, i.e. by a *quasi–static* evolution of droplet shapes. Throughout this work we employed the public domain software Surface Evolver[27,28] to compute static droplet shapes by numerical energy minimization. In accord with our experimental conditions, we assume a homogeneous microscopic material contact angle, or equivalently homogeneous material advancing / receding angles,

and minimize the interfacial energy under the global constraint of a constant liquid volume. Surface topographies are explicitly modelled via periodically repeated local constraints that enforce the nodes of the contact line to follow the specific cross–sectional geometry of the linear grooves. Because we assume the droplets to be small compared to the capillary length, we will neglect the influence of gravity or buoyancy.

Special care is taken in the explicit droplet model while the interface is displaced over non–smooth parts of the substrate. During the energy minimizations, we need to reassign, if necessary, the nodes of the contact line on the discontinuity to the respective constraint representing the smooth surfaces to one or the other side. These operations are applied according to the condition of Young–Dupré and the local slope of the liquid interface, and guarantee that both pinning and de–pinning of the contact line at acute edges conforms to the Gibbs criterion.[6,20,22]

Typically, the droplet volume is enlarged in small increments, each time followed by a sufficient number of minimization steps. To help the minimization dynamics, especially for the growth of long filament, at each discrete volume increment ΔV, an homothety of the longitudinal coordinate y of nodes is applied: $y' = (1 + \Delta V/AL_\parallel)y$ where A is the area of the perpendicular cut of the drop morphology in its symmetry center. Along the grooves the full domain is simulated, to allow symmetry breaking and non symmetric transitions when invading a near groove. When spilling occurs, the side where it happens is randomly chosen each time by numerical noise. The optimal number of steps is determined by a convergence criterion based on energy and the maximum displacement among all vertices. In this way, we ensure that the interfacial configuration remains close to a local energy minimum. Specifically, our procedure prevents unexpected transitions from filament to bulge morphologies, which might occur as consequence of inaccurate minimisation procedure. Once the interfacial shape for the given volume is sufficiently close to such a local minimum, we extract the geometry of the base length $L_\parallel$ and width $L_\perp$, the apparent contact

angles $\theta_\perp$ in the head–on view of droplet and $\theta_\parallel$ in side view, c.f. the indicated contact angles and base lengths in Fig. 1(d–f). This protocol allows us to follow the quasi–static evolution of a droplet that is initially located within a few grooves until it covers more than a hundred grooves. A similar approach has been employed to study interfaces advancing over a square array of cylindrical posts.[29,30]

3   Growth modes

To begin our analysis, in this section we provide a phenomenological description of the droplet growth on linear v–groove topographies. However, the majority of arguments in the remainder of this article not only apply to droplets on arrays of periodically repeated v–grooves, but also to droplets on a much wider class of periodic linear micro–patterns with a continuous translation symmetry, i.e. grooves with other cross–sections or patterns of chemical stripes. Two qualitatively different shape evolutions are encountered. These growth modes are consistently found both in our wetting experiments and in our numerical energy minimizations. Characteristic for the first growth mode is a continuous increase of the droplet's extension $L_\parallel$ into the direction of the grooves. During spreading, the liquid remains in contact to a constant number of grooves and forms a 'liquid filament' of fixed width $L_\perp$. Examples of filaments observed in numerical energy minimizations and in experiments are shown in panel (a) and (c), respectively, of Fig. 1. Because the lateral segments of the three-phase contact lines remain pinned to the ridges of the v–grooves during volume growth, the width $L_\perp$ of filament is necessarily an integer multiple of the period W of the groove pattern. Since $L_\perp$ is fixed the base eccentricity

$$\varepsilon = \frac{L_\parallel - L_\perp}{L_\parallel + L_\perp} \ , \qquad (1)$$

of a growing filament tends to unity, as illustrated by the plot of ε a function of time in Fig. 1(g) for the experimentally recorded filament shown in Fig. 1(c).

In contrast to the unidirectional growth mode, the liquid of the growing droplet may also spread in an alternating fashion parallel or perpendicular with respect to the groove direction. The alternating growth becomes manifest in oscillations of the base eccentricity ε as plotted in Fig. 1(g) for the droplet shown in Fig. 1(c). Characteristic for this 'bidirectional growth mode' are periods of a continuous elongation of the droplet shape into the groove direction interrupted by regularly recurring fast rearrangements of the lateral interfaces. These events are visible as the downward jumps in the base eccentricity, as illustrated by the example Fig. 1(g) for the particular droplet shown in Fig. 1(c).

To gain further insight into the factors that control the morphological evolution of liquid droplets on linear grooves, we will first consider droplets in contact to only a small number of grooves. In view of the wetting experiments on samples molded from anisotropically etched Si–wavers, we will restrict our discussion to the particular example of v–grooves with a slope angle of $\psi = 54.7°$.

Droplets with the free interface forming a portion of sphere and wetting the bottom of one v–groove exist as stable shapes for small liquid volumes $V \ll \mathcal{O}(W^3)$, where W is the width of a single v–groove, c.f. also the rendering in Fig. 3(a). To prevent complete spreading in the bottom of the v–grooves, the material contact angle must satisfy the inequality $\theta_0 > \psi$.[31] During volume growth, the outermost lateral parts of the three–phase contact line will become pinned to the top of the ridge separating two adjacent grooves. After this point, the growing droplet may evolve either into a filament for small material contact angles, or into a localized droplet for larger material contact angles, as shown in Fig. 3(b) and (c), respectively. For the latter case, in response to a further volume increase the lateral three-phase contact lines will de–pin and move on the slopes of the adjacent grooves once Gibbs' criterion $\theta_\perp < \theta_a = \theta_0 + \psi$ is violated.[20,22] Excursions of the droplet's three–phase contact line onto the slopes of the neighboring grooves can be still found in mechanical equilibrium, as illustrated
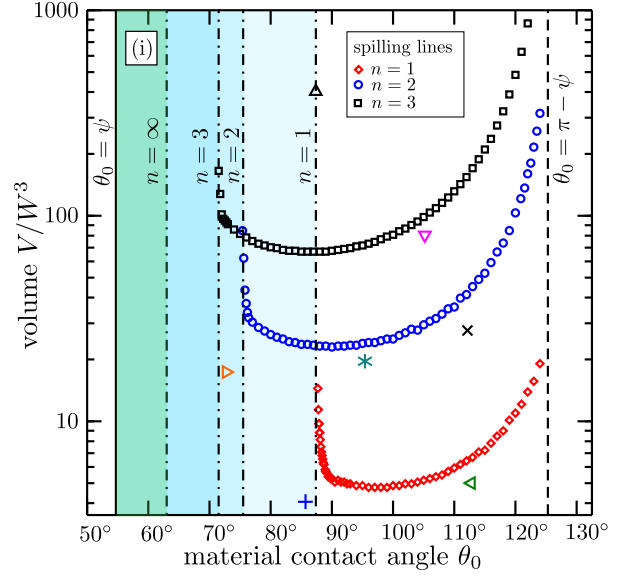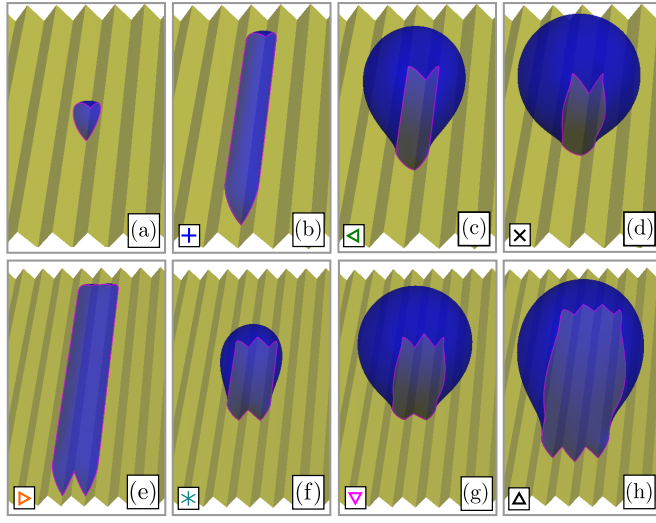
Figure 3: Droplet morphologies in contact to v–grooves with a slope angle of $\psi = 54.7°$ for various material contact angles θ_0 and dimensionless liquid volumes V/W^3. Shown are numerical energy minimizations of a spherical droplet (a) for $(\theta_0, V/W^3) = (90°, 0.32)$, a filament (b) confined to a single v–groove for $(85°, 4)$, a droplet (c) with pinned contact line for $(112°, 5)$, and a droplet (d) with a de-pinned contact line for $(112°, 28)$. The second row displays a liquid filament (e) wetting two v–grooves for $(73°, 17.5)$, a droplet (f) with pinned contact line wetting two grooves for $(95°, 20)$, a droplet (g) with de–pinned contact line wetting two grooves $(105°, 80)$, and (h) wetting three grooves for $(87°, 130)$. (i): Spilling lines for droplets wetting $n = 1$, 2, 3 grooves in terms of the material contact angle θ_0 and dimensionless volume V/W^3.

in Fig. 3(d).

The dimensionless volume V/W^3, at the point of de–pinning as a function of the material contact angle θ_0 defines a 'spilling line'. Numerically computed values are displayed in the diagram Fig. 3(i). Apparently, the dimensionless rescaled volume V/W^3 on the spilling line in Fig. 3(i) diverges when approaching a material contact angle $\theta_0 = 87.5°$ from above. An analogous observation is made for the spilling lines of droplets wetting two or more v–grooves. Inspection of Fig. 3(i) reveals that the spilling line diverges at a material contact angle $\theta_0 = 75.4°$ for two and at $\theta_0 = 71.4°$ for three wet grooves. Generally, the material contact angle at the point of divergence is the lower the larger the number of wet grooves.

Toward larger material contact angles, all three numerically determined spilling lines in Fig. 3(i), i.e. for droplets wetting one, two, or three v–grooves, diverge at the same material contact angle $\theta_0 \approx 124°$. At higher material contact angles, $\theta_0 > \pi - \psi = 124.3°$, the lateral contact angle $\theta_\perp$ must reach a value larger than π to de–pin from the ridges and to move onto the side walls of the v–grooves. Effectively, the three–phase contact line cannot de–pin during volume growth if the material contact angle θ_0 is larger than 124.3°. Interestingly, we observe a transition from the Wenzel to the supended Cassie state on the v–grooves as θ_0 exceeds ψ.

Results of numerical energy minimizations of the explicit model for a series of wedge angle ψ between 10° and 30° in Fig. 4(a) demonstrate that oscillations continue also for droplets wetting a large number of grooves $n \sim \mathcal{O}(100)$, albeit with a progressively decreasing amplitude. Each discontinuous jump of the base eccentricity to a smaller value correlates to an increment of n by one, as illustrated by the comparison of experimentally measured and numerically computed values of ε in Fig. 4(a). Similar to the base eccentricity, the apparent contact angle $\theta_\perp$ in head–on view approaches the de–pinning angle $\theta_a = \theta_0 + \psi$ in an oscillatory manner from below. The amplitude of the oscillations in $\theta_\perp$ also decreases as the number n of wet grooves increases.

Experimentally measured base eccentricities ε of growing droplets shown in Fig. 4(b) as a function of the number of wet grooves n support that shape oscillations during bidirectional growth become smaller as n increases. Corresponding images in top view Fig. 4(b) illustrate that the global shapes of droplets undergoing bidirectional growth tend to a smooth limiting shape. Corrugations close to the three–phase contact line scale with the order the period W of the grooves and become increasingly irrelevant in relation to the droplet size in the limit of large volumes $V/W^3 \gg 1$. In both the explicit numerical model and in our wetting experiments, the apparent contact angle $\theta_\parallel$ approaches the Wenzel angle

$$\theta_w = \arccos\left(r\cos\theta_0\right) \qquad (2)$$

in the limit $n \to \infty$ of asymptotically wide droplets, where $r = 1/\cos\psi$ is the ratio of the true surface area to the projected substrate area on the grooves. The apparent angle $\theta_\parallel$ in a side–view is identical to the Wenzel angle not only for wide droplets in the bidirectional growth regime and applies also to wide filaments in the limit $n \to \infty$. This equality $\theta_w = \theta_\parallel$ is expected because all parts of the interface where three-phase contact line is not aligned with the direction of the grooves can locally relax into a state of minimum energy.

Since the contact line is mostly advancing during volume growth, the presence of a small contact angle hysteresis in the experiment can be in first approximation neglected, assuming that the material contact angle can be replaced by the static advancing contact angle.[32] This approximation will be inaccurate when during the quick spilling from a reduced number of grooves, by volume conservation, the liquid at the extrema can be slightly pulled back. In practice the presence of a small hysteresis will cause a decrease of the contact angle instead of a receding motion of the contact line. Further volume flux will restore the advancing condition before the drop further expands. This finite size effect quickly is suppressed as the number of occupied grooves increases.

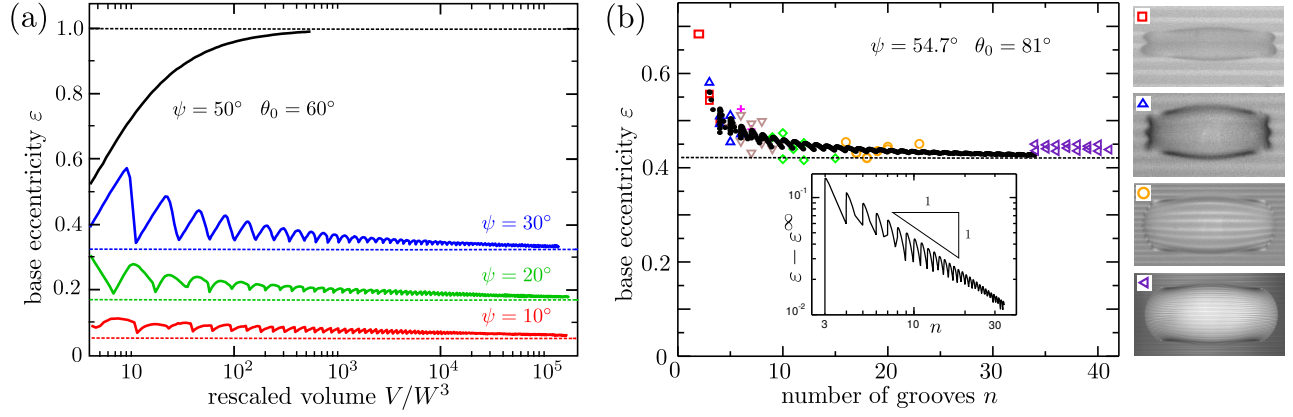The base eccentricity ε of droplets wetting a finite number of grooves is typically larger than

Figure 4: (a): Numerically calculated base eccentricities ε of droplets growing on v–grooves with material contact angle $\theta_0 = 60°$ and various slope angle ψ as function of droplet volume V in units of the groove width W. Initial droplet shapes are in contact to only two v–grooves. Dashed lines in (a) and (b) indicate the corresponding asymptotic value ε^∞ of the plane stripe model, c.f. also Fig. 7 (b). (b): Droplet base eccentricity, ε, as a function of the number n of wet v–grooves for material contact angle $\theta_0 = 81°$ and slope angle $\psi = 54.7°$. Open symbols represent experimental data from different droplets in comparison to our numerical data (black points). Example droplet shapes of data sets are shown in the right column. Inset: Finite size scaling of the base eccentricity ε as a function of the lateral size of the numerically computed droplet shape for material contact angle $\theta_0 = 81°$ and slope angle $\psi = 54.7°$.

the asymptotically reached base eccentricity ε^∞ for $n \to \infty$, c.f. the comparison of numerical and experimental data shown in Fig. 4(a) and (b). As expected, the amplitude of the shape oscillations of droplets decreases with an increasing volume. Plotting the difference $\varepsilon - \varepsilon^\infty$ of the actual base eccentricity ε of a droplet undergoing bidirectional growth and its asymptotic value ε^∞ in the inset of Fig. 4(b) reveals an asymptotic scaling $\sim n^{-1}$ when plotted against the number of wet grooves n. Finite size scaling with the number of wet grooves is not only observed for droplets in the bidirectional growth regime but also for liquid filaments, as will be shown in the following section.

4   Filament stability

To better understand the origin and the coexistence of the two growth modes, we will now formulate a criterion for the appearance and mechanical stability of asymptotically long liquid filaments with $L_\parallel \gg W$. The criterion can be derived from simple geometrical considerations. Following the method applied in Ref.,[23] we assume that the liquid filament exhibits a ho-

mogeneous cross–section and extends between two movable walls. The lateral segments of the contact line shall be pinned to the top of the ridges. To be consistent with the assumption of a homogeneous cross–section, the liquid interface must form a contact angle of $\theta_0 = \pi/2$ with the movable walls. The orientation of the walls shall be perpendicular to both the substrate and the direction of the v–grooves. Mechanical equilibrium of the liquid demands that the free interface is a segment of a cylinder, i.e. the contour of the interface in a plane cut perpendicular to the long side is a circular arc with an opening angle of $0 < \theta_\perp \le \pi$.

The condition for a mechanical equilibrium of a liquid filament subject to variations of its length takes on the form:

$$\gamma_{lv} \left(L_{lv} - \cos\theta_0\, L_{ls} \right) = P A_l \ , \qquad (3)$$

where γ_{lv} and L_{lv} denote the interfacial energy and contour length of the liquid–vapor interface, respectively, L_{ls} the contour lengths of the wet substrate, while P is the Laplace pressure and A_l the area of the liquid in a plane cross–section of the filament perpendicular to the v–

9

grooves.

For the particular case of a filament spanning n v–grooves of width W, we find:

$$A_l = \left(\frac{\theta_\perp - \sin\theta_\perp \cos\theta_\perp}{4\sin^2\theta_\perp} + \frac{\tan\psi}{4n} \right) n^2 W^2 \ , \quad (4)$$

while the Laplace pressure of the cylindrical liquid–vapor interface reads:

$$P = \frac{\gamma_{lv}}{R} = \frac{2\gamma_{lv}\sin\theta_\perp}{nW} \ . \quad (5)$$

The respective contour lengths of the interfaces in a cross–section of the filament are given by:

$$L_{lv} = \frac{nW\theta_\perp}{\sin\theta_\perp} \qquad \text{and} \qquad L_{ls} = \frac{nW}{\cos\psi} \ . \quad (6)$$

After inserting expressions (4), (5), and (6) into the equilibrium condition (3), we eventually arrive at the implicit condition:

$$\frac{\cos\theta_0}{\cos\psi} = \frac{\theta_\perp}{2\sin\theta_\perp} + \frac{\cos\theta_\perp}{2} - \frac{\sin\theta_\perp \tan\psi}{2n} \quad (7)$$

for mechanically equilibrated cylindrical filaments wetting n v–grooves with a slope angle ψ. Note, that the lhs of Eqn. (7) is the cosine of Wenzel angle on of grooved substrate.

In terms of the apparent contact angle $\theta_\perp$, the equilibrium condition Eqn. (7) has either two real solutions or no real, i.e. no physically meaningful solution. This can be easily demonstrated by solving Eqn. (3) for the material contact angle θ_0 which is then a function of the lateral contact angle $\theta_\perp$, the number of wet grooves n, and the slope angle ψ. Since the material contact angle θ_0 as a function of $\theta_\perp$ for fixed n and ψ displays a single maximum θ_0^{max} at $\theta_\perp = \pi/2$, and we conclude that condition Eqn. (7) has two solutions in $\theta_\perp$ if $\theta_0 < \theta_0^{max}$, exactly one if $\theta_0 = \theta_0^{max}$, and no solution if $\theta_0 > \theta_0^{max}$. The maximum material contact angle allowing aymptotically long filaments to be mechanically stable is then

$$\theta_0^{max}(\psi, n) = \arccos\left(\frac{\pi}{4}\cos\psi - \frac{\sin\psi}{2n} \right), \quad (8)$$

and depends only on the slope angle ψ of the v–grooves and the number n of wet grooves.

Further analysis shows that the solution branch of Eqn. (7) with the smaller contact angle $\theta_\perp = \theta_\perp^s(\psi, n, \theta_0)$ corresponds to liquid filaments that are stable with respect to variations of their length while the solution with the larger contact angle $\theta_\perp = \theta_\perp^l(\psi, n, \theta_0)$ always corresponds to unstable equilibria. Stability of the liquid–vapor interface with respect to the Plateau-Rayleigh instability at fixed length is guaranteed for the condition $\theta_\perp < \pi/2$ which is always satisfied by the small solution branch $\theta_\perp^s(\psi, n, \theta_0)$. This finding agrees with the stability analysis of liquid filaments wetting a plane chemical stripe that is surrounded by a perfectly non–wetting surface.[3,23]

For the present case of v–grooves, the Gibbs criterion imposes a further restriction to the set of mechanically stable filaments. Pinning of the contact line to the top of the ridges requires that the inequality $\theta_\perp < \theta_a = \theta_0 + \psi$ is fulfilled. According to the model predictions of Eqn. (7), the the stability boundary $\theta_0^{max}(\psi, n)$ indeed satisfies $\theta_0^{max}(\psi, n) + \psi > \pi/2$ for any number of wet grooves n if the slope angle is $\psi = 54.7°$.

To verify the predictions of the filament model with the results of the energy minimizations presented in Sec. 3, we plot the values of $\theta_0^{max}(\psi, n)$ computed from Eqn. (7) as vertical lines in the stability diagram Fig. 3(g). All values $\theta_0^{max}(54.7°, 1) = 87.38°$, $\theta_0^{max}(54.7°, 2) = 75.43°$, and $\theta_0^{max}(54.7°, 3) = 71.47°$, are in very good agreement with the points where the numerically determined spilling lines for droplet wetting a corresponding number of v–grooves diverge. The observation that the region of mechanically stable filaments with finite size is enlarged explains the experimental observation of unidirectional growth of condensing water droplets on a fresh NOA81 surface with an advancing material contact angle of $\theta_0 = (70 \pm 4)°$, c.f. the filament wetting three grooves in Fig. 3(c). While we expect to find only droplets in the bidirectional growth regime for a wedge angle of $\psi = 54.7°$ and $n \to \infty$, the experimentally determined value of the advancing material contact angle on the fresh NOA81 is consistent with the range of values where a filaments spanning three v–grooves are mechanically stable.
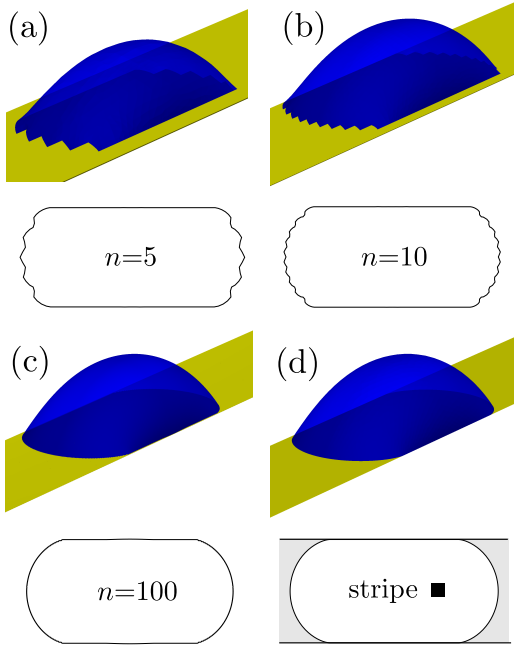
Figure 5: (a–c): Numerically computed droplet shapes and contours of the three phase contact line for droplets on v–grooves in the explicit model for a different number n of wet grooves. Wedge angle and material contact are $\psi = 30°$ and $\theta_0 = 60°$, respectively. (d): Equivalent droplet morphology on a plane stripe with $\theta_\perp = 90°$ and $\theta_\parallel = 54.7°$. Rescaled volume and confinement parameter are $V/L_\perp^3 = 4.95$ and $\xi = 0.729$, respectively, for all droplets shown here.

The range of material contact angles that permit stable liquid filaments wetting an arbitrary large number of grooves is limited by $\theta_0^{max}(54.7°, \infty) = 63.01°$ which corresponds to a Wenzel angle of $\theta_w = \arccos(\pi/4) = 38.24°$. This angle is identical to the largest material contact angle that permits mechanically stable liquid filaments that are confined to a plane chemical stripe.[23,24] As we are going to show in the next section, this analogy is not accidental and can be further exploited to formulate a consistent model for the appearance of certain growth modes for asymptotically wide droplets, i.e. in the limit $n \to \infty$.

5   Plane stripe model

In this section we will present a detailed model

able to predict morphologies of drops growing on linear patterns in the limit of covering a large number of linear features. A closer inspection of the droplet shapes recorded in our experiments and numerical energy minimizations reveals that not only the base eccentricity ε converges to a finite value ε^∞, but also the entire shape of an oscillatory growing droplet tends to a scale–invariant limit shape. Apparently, the global shape of the droplet wetting v–shaped grooves in the example Fig. 5(a–c) approaches the shape of the droplet on a chemical stripe displayed in Fig. 5(d) for $n \to \infty$. The latter droplet adheres to a plane stripe with a uniform material contact angle $\theta_\parallel$ which is identical to the Wenzel angle θ_w of the liquid on the v–grooves [1]. In contrast to the ridges of the linear v–grooves, the boundaries of the plane stripe act as complete wetting barriers for the liquid and do not permit a detachment of the three phase contact line. Hence, the width of a droplet on the wettable stripe is fixed to the stripe width $L_\perp$ while the contact angle $\theta_\perp$ adjusts itself based on the rescaled volume and the contact angle of the stripe $\theta_\parallel$.

Identical droplet shapes on a grooved substrate and on a chemical stripe not only demand that the Wenzel angle θ_w on the grooved substrate equals the contact angle $\theta_\parallel$ on the stripe but also that the rescaled volumes $V/L_\perp^3$ of both droplets are the same. The converse statement, however, may not be true, as equilibrium shapes on a chemical stripe are not uniquely determined by the material contact angle $\theta_\parallel$ and the rescaled droplet volume $V/L_\perp^3$.[23,24] In the following we will demonstrate that shapes in the range of mechanically bistable droplet morphologies can be unambiguously distinguished by the lateral contact angle $\theta_\perp$. This particular order parameter plays a pivotal role for the shape evolution of droplets growing on linear patterns. With the exception of transient states immediately after de–pinning, the lateral parts of the interface are pinned to the ridges or chemical boundaries, and therefore the apparent contact angle $\theta_\perp$ must always be equal to or

---

[1]Note, that the apparent contact angle in side view $\theta_\parallel$ is identical to the Young's contact angle θ_0 on the wettable stripe.

smaller than the de–pinning angle θ_a. Matching the lateral contact angle $\theta_\perp$ of the droplet on the stripe to the angle θ_a of the grooved substrate, provides us with the shapes of asymptotically wide droplet in the bidirectional growth regime.

The condition $\theta_\perp \leq \theta_a$ in form of an inequality opens the possibility that any droplet shape on a chemical stripe can represent a wide droplet undergoing bidirectional growth with $\theta_\perp = \theta_a$ on one substrate and, at the same time, a unidirectionally growing droplet on another substrate. While the Wenzel angle θ_w is the same on both substrate, the de–pinning angle on the latter satisfies $\theta_a > \theta_\perp$.

5.1 Droplet morphologies on a chemical stripe

Similarly to what observed for v-grooved linear patterns, also for a single wettable stripe drops can adopt filament of bulged shapes. Before deriving the explicit map, in this subsection we will revisit the main results on the spectrum of equilibrium droplet shapes on a wettable stripe that is surrounded by a fully non–wetting surface.[23,24]

Besides the uniform material contact angle on the plane stripe, $\theta_\parallel$, the droplet shape is determined by the dimensionless volume $V/L_\perp^3$, where $L_\perp$ is the width of the stripe. For the purpose of the present work, we will employ the degree of lateral confinement

$$\xi = \frac{L_c - L_\perp}{L_c} \tag{9}$$

instead of $V/L_\perp^3$, where

$$L_c = \left[\frac{24V \sin^3 \theta_\parallel}{\pi(1 - \cos\theta_\parallel)^2(2 + \cos\theta_\parallel)} \right]^{\frac{1}{3}} \tag{10}$$

is the diameter of the contact line of an unconfined spherical cap–shaped 'reference droplet'. The latter droplet comprises the same volume V as the confined droplet but wets a plane and homogeneous surface with the same contact angle $\theta_\parallel$. By construction, the dimensionless confinement parameter defined by Eqns. (9,10) is always between zero and one. Figure 6 displays
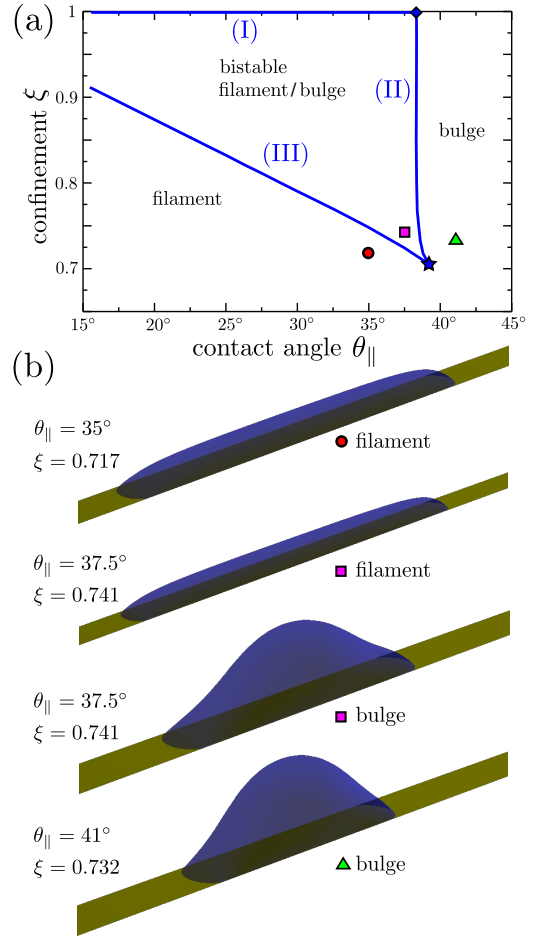

(a)

(b)

$\theta_\parallel = 35°$
$\xi = 0.717$ • filament

$\theta_\parallel = 37.5°$
$\xi = 0.741$ ■ filament

$\theta_\parallel = 37.5°$
$\xi = 0.741$ ■ bulge

$\theta_\parallel = 41°$
$\xi = 0.732$ ▲ bulge

Figure 6: (a): Stability diagram of possible droplet morphologies on a plane stripe with contact angle $\theta_\parallel$ and the dimensionless confinement parameter ξ, c.f. also the definitions Eqns. (9) and (10). A bistability between elongated and spread–out filamentous shapes and localized, bulge–like shapes are found in shaded region for the same values of the control parameter $\theta_\parallel$ and ξ. (b): Examples of bulge and filament morphologies on a wettable stripe.

the stability diagram of droplets shapes on the plane stripe in terms of the contact angle $\theta_\parallel$ on the stripe and the confinement parameter ξ.

A mechanical bistability between filament and bulge droplets is found in the triangular region bounded by three almost straight lines denoted by (I), (II), and (III). Right of the filament stability line (II) in Fig. 6, only bulge–like droplets are found while below line (III), only filamentous droplets can exist as mechanically stable configurations. The stability lines

12

for filaments, (II), and for bulges, (III), emerge from the bifurcation point $(\theta_{\parallel}^{\star}, \xi^{\star})$, indicated by the star symbol ($\star$) in Fig. 6, where the difference between the two morphologies vanishes. The contact angle at the bifurcation point is determined from numerical computations as $\theta_{\parallel}^{\star} \simeq 39.2°$.[23,33] Asymptotically long liquid filaments on the plane stripe exist as stable shapes only for contact angles

$$\theta_{\parallel} < \theta_{\parallel}^{\blacklozenge} = \arccos\left(\frac{\pi}{4}\right) \simeq 38.24° \ , \qquad (11)$$

which implies that the filament stability line (II) terminates in the point $(\theta_{\parallel}, \xi) = (\theta_{\parallel}^{\blacklozenge}, 1)$ as shown by the filled diamond symbol ($\blacklozenge$) in Fig. 6.

Since arbitrarily long filaments with $\xi \to 1$ exist on a wettable stripe for arbitrarily small contact angles $\theta_{\parallel} \leq \theta_{\parallel}^{\blacklozenge}$, the region of stable filaments in Fig. 6 is bounded by line (I) which extends to the point $(\theta_{\parallel}, \xi) = (0, 1)$. Asymptotically long liquid filaments with $\xi \to 1$ exhibit a homogeneous cylindrical cross–section. The lateral contact angle $\theta_{\parallel}$ of mechanically stable long filament necessarily satisfies $\theta_{\perp} < \pi/2$.[3,23]

5.2 Mapping of shapes

To identify droplet shapes on the wettable stripe with suitable shapes of droplets growing on a pattern of linear grooves, we need to determine the lateral contact angle $\theta_{\perp}$ of mechanically equilibrated droplets on the stripe for any pair of contact angle $\theta_{\parallel}$ and confinement parameter ξ. Using the numerically computed droplet shapes on a chemical stripe we are able to express the lateral contact angle as a function $\theta_{\perp} = g(\theta_{\parallel}, \xi)$ that is either a single–valued function, or exhibits two branches if the contact angle $\theta_{\parallel}$ and confinement parameter ξ fall into the region of bistability in the diagram shown in Fig. 6.

Each branch $g_{\alpha}(\theta_{\parallel}, \xi)$ corresponds to the lateral contact angle $\theta_{\perp}$ of either bulges ($\alpha = b$) or filaments ($\alpha = f$). To our surprise, the set of numerically computed droplet shapes reveals that any pair of contact angles $(\theta_{\parallel}, \theta_{\perp}) \in [0, \pi] \times [0, \pi]$ is attained for at most one stable equilibrium

shape. The injectivity of the map $\theta_{\perp} = g(\theta_{\parallel}, \xi)$ implies that any droplet shape on the plane stripe, and, by our central hypothesis, on any periodic pattern of linear grooves, is unambiguously identified by the pair of apparent contact angles $(\theta_{\parallel}, \theta_{\perp})$ in side view and head–on view, respectively. By virtue of this 'unfolding', the confinement parameter becomes a single–valued function $\xi = \tilde{g}(\theta_{\parallel}, \theta_{\perp})$. Analogous statements apply to any quantity that is related to only the droplet shape, including the base eccentricity ε.

Density plots of the confinement parameter $\xi = \tilde{g}(\theta_{\parallel}, \theta_{\perp})$ for droplets on the chemical stripe and the corresponding base eccentricity ε are shown in Fig. 7. Apparently, the map $\theta_{\perp} = g(\theta_{\parallel}, \xi)$ is not surjective, i.e. the droplet shapes on the wettable stripe do not attain all possible pairs of angles $(\theta_{\parallel}, \theta_{\perp}) \in [0, \pi] \times [0, \pi]$. Besides the trivially excluded region with $\theta_{\perp} < \theta_{\parallel}$, we could not detect any stable shape in the gray shaded region of the plots shown in Fig. 7. The latter region of contact angles pairs $(\theta_{\parallel}, \theta_{\perp})$ is enclosed by the mapped boundary of the bistable region found in the morphology diagram Fig. 6, i.e. by the image of lines (I) and (II) under $g_f(\theta_{\parallel}, \xi)$ and the image of the boundary line (III) under $g_b(\theta_{\parallel}, \xi)$. The boundary curve (I) can be parameterized by the function $\theta_{\perp} = g_f(\theta_{\parallel}, 1)$ with $\theta_{\parallel} \in [0, \theta_{\parallel}^{\star}]$, as given in implicit form by Eqn. (7) in the limit $n \to \infty$ or, equivalently, by Eqn. (18) in Ref.[23] As a consequence of the excluded region shown in gray, the range of possible lateral contact angles of droplet with a given $\theta_{\parallel}$ exhibits a gap for $\theta_{\parallel} < \theta_{\parallel}^{\star}$ which progressively widens as $\theta_{\parallel} \to 0$.

The second important observation made for numerical computed droplet shapes on a chemical stripe is the strict monotonicity of the lateral contact angle $\theta_{\perp} = g(\theta_{\parallel}, \xi)$ and the monotonicity of the corresponding inverse function $\xi = \tilde{g}(\theta_{\parallel}, \theta_{\perp})$. In any case, the lateral angle $\theta_{\perp}$ of a droplet at a fixed contact angle $\theta_{\parallel}$ on the chemical stripe grows monotonously during an increase of the confinement parameter ξ. Only when approaching line (II) and (III), the derivatives $\partial_{\xi} g_b(\theta_{\parallel}, \xi)$ and $\partial_{\xi} g_f(\theta_{\parallel}, \xi)$ diverge.
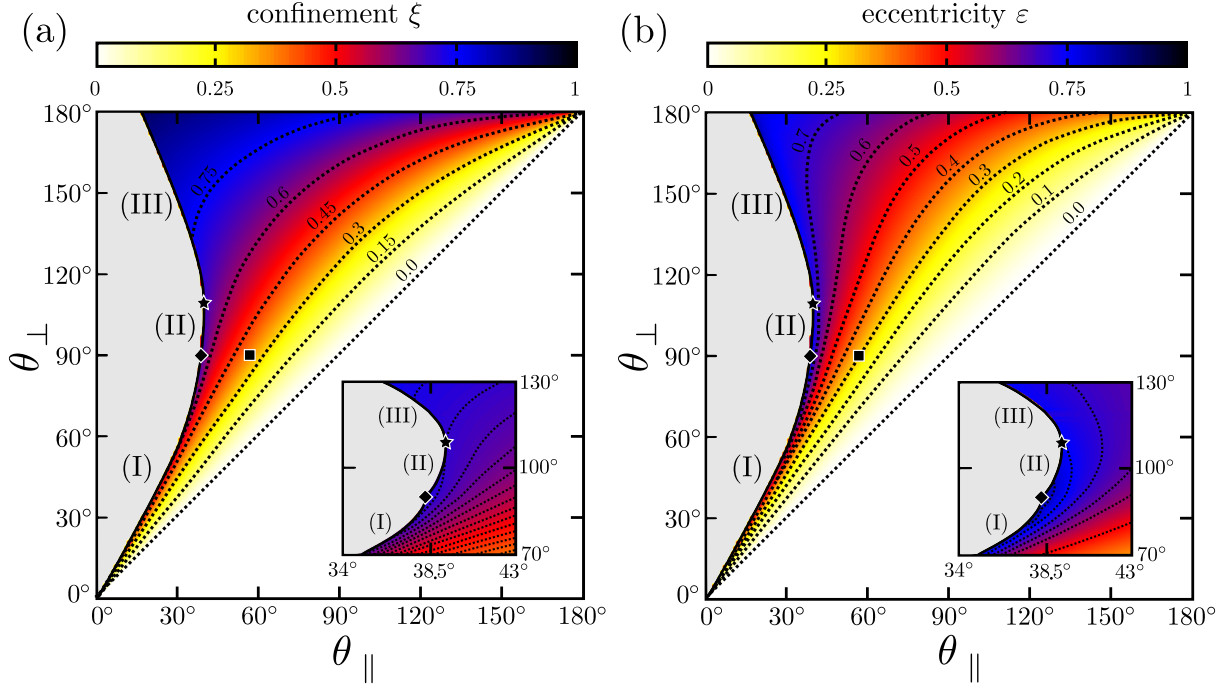
Figure 7: Universal plot of (a) the confinement parameter ξ and (b) base eccentricity ε in terms of the apparent contact angles $\theta_\parallel$ and $\theta_\perp$, c.f. also Fig. 1. The square symbol (■) indicates the droplet shown in Fig. 5 (a). Curves denoted by (I), (II) and (III) as well as the points denoted by star (★) and diamond (◆) are mapped from the corresponding to curves and points in diagram Fig. 6.

5.3 Shape evolution and growth regimes

Equipped with the unfolding of the stability diagram Fig. 6 generated by a coordinate transformation from $(\theta_\parallel, \xi)$ to $(\theta_\parallel, \theta_\perp)$, we will now turn to our initial aim which is to explain the wetting behavior of growing droplets in contact to a large number of v–grooves.

Supported by our central observation, we find asymptotically wide droplets in the bidirectional growth regime if the pair of *substrate specific* contact angle (θ_w, θ_a), matches a pair of *droplet specific* apparent contact angles $(\theta_\parallel, \theta_\perp)$ of a droplet on the chemical stripe. This is the case in region denoted by (B) in the plane of contact angles (θ_w, θ_a) in the schematic diagram Fig. 8. Unidirectional droplet growth, however, can be observed if the condition $\theta_\perp < \theta_a$ holds for arbitrarily large liquid volumes. This condition can only be satisfied by growing liquid filaments in region (U) above the filament line (I) in Fig. 8. History dependence of droplet shapes becomes manifest as regions (U/B) and (U/B*) where both unidirectional

and bidirectional droplet growth could be encountered on the same substrate. In contrast to the regular bidirectional growth (B) above the filament line (I) in Fig. 8, we find a specific region (B*) above line (II) where the droplets on the grooved surface may grow in an irregular way.

To illustrate, and to explain the underlying physical mechanisms that control the occurrence of the growth modes described above, we will follow the shape evolution during an increasing volume for different Wenzel angles θ_w. In each instance, neglecting finite size effects near the contact line, we assume an initially spherical droplet that is already in contact to a large number of grooves. In this case, the apparent contact angle of the spherical caps must be equal to the Wenzel angle and thus correspond to points on the diagonal $\theta_\perp = \theta_\parallel$ in Fig. 8.

5.3.1 Large Wenzel angle $\theta_w \geq \theta_\parallel^\star$

Let us first consider the case of large Wenzel angles above the bifurcation point, $\theta_w > \theta_\parallel^\star$. A growth of the initially spherical droplet en-
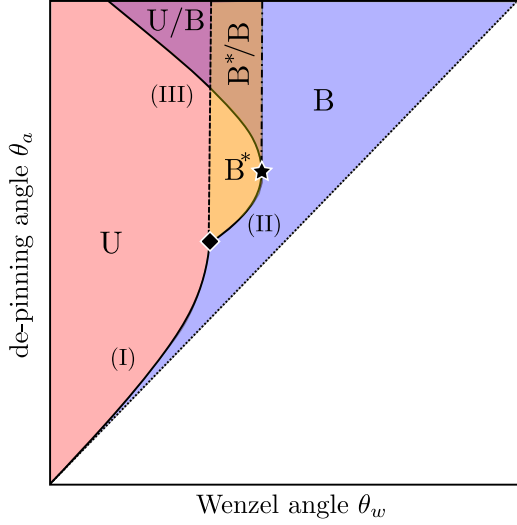
14

Figure 8: Schematic illustration of growth modes on linear surface grooves with Wenzel angle θ_w and de–pinning angle θ_a (not to scale). Shown are the unidirectional growth regime (U), the regular bidirectional growth regime (B), and the irregular bidirectional growth regime (B*). The specific points indicated by symbols ($\star$) and ($\blacklozenge$) are located at $(\theta_w, \theta_a) = (39.2°, 109°)$ and $(38.25°, \pi/2)$, respectively.

tails not only an increase of the droplet extension $L_\parallel$ parallel to the grooves, but also an increase of the lateral contact angle, $\theta_\perp$. As long as $\theta_\perp$ is smaller than the de–pinning angle θ_a, the lateral contact line segments remain pinned and the droplet width $L_\perp$ remains constant. As a consequence, the confinement parameter ξ grows during an increase of the liquid volume. Only when the de–pinning condition $\theta_\perp = \theta_a$ is reached, the droplet width $L_\perp$ increases by one period W of the groove pattern. Because transverse spreading leads to a slight relaxation of ξ, and consequently, to a decrease of $\theta_\perp$, the pinning condition $\theta_\perp < \theta_a$ will be restored after the jump. Further volume growth leads to a continuous increase of the lateral contact angle $\theta_\perp$ and confinement parameter ξ, and a subsequent de–pinning event will be triggered once the de–pinning condition $\theta_\perp = \theta_a$ has been reached again.

Over time, we will observe a step–wise transverse growth of the droplet while the lateral contact angle $\theta_\perp$ approaches θ_a in an oscillatory manner, c.f. the examples shown in Fig. 4. Ir-

respective of the de–pinning angle θ_a, droplets with a Wenzel angle $\theta_w > \theta_\parallel^\star$ display bidirectional growth (B).

5.3.2 Small Wenzel angle $\theta_w \leq \theta_\parallel^\blacklozenge$

The evolution of droplet shapes for small Wenzel angles θ_w below $\theta_\parallel^\blacklozenge$ is identical to the scenario for $\theta_w > \theta^*$ explained above, provided the depinning contact angle θ_a is *smaller* than $\theta_\perp$ on the boundary (I) in the diagram in Fig. 8. In this region, we find exclusively droplets in the bidirectional growth mode (B).

If the pair of contact angles (θ_w, θ_a) lies in the region (U) or (U/B) of the diagram Fig. 8, the de–pinning condition of the growing droplet cannot be reached and the liquid spreads only into the direction of the grooves. At the same time, the lateral contact angle $\theta_\perp$ converges monotonously to the asymptotic value $\theta_\perp \to g_f(\theta_w, 1) < \pi/2$ on line (I), describing asymptotically long filaments.

Both, scale–invariant shapes of droplets in the bidirectional growth mode and liquid filaments in the unidirectional growth mode are possible for contact angle pairs (θ_w, θ_a) in the region of Fig. 8 denoted by (U/B). Here, the bidirectional growth regime cannot be reached by a continuous increase of the liquid volume if we start from a spherical cap–shaped droplet. In this case, the droplet will always continue to grow into the direction of the grooves. To initiate bidirectional growth, the droplet has to overcome the energy barrier that separates the stretched–out filament from the localized droplet for the given Wenzel angle θ_w, width $L_\perp$, and volume V.

Only the bulge conformation satisfies the condition $\theta_\perp = \theta_a$ that is necessary for bidirectional growth. A continuous decrease of the Wenzel angle for a fixed V and $L_\perp$, e.g. by electrowetting[24] could be used to prepare localized droplets undergoing bidirectional growth in the region (U/B) of Fig. 8. But even then, an observation of bidirectional droplet growth in the region (U/B) will be very hard to achieve in experiments, because one needs a small Wenzel angle while the de–pinning angle must be close to π. For substrates with v–grooves, this would

imply large slope angles close to $\pi/2$.

5.3.3 Intermediate Wenzel angle $\theta_\parallel^\bullet \leq \theta_w \leq \theta_\parallel^\star$

Droplets in narrow region of Wenzel angles θ_w between $\theta_\parallel^\bullet$ and $\theta_\parallel^\star$ below line (II) in the diagram Fig. 8 display a bidirectional growth. However, for contact angle pairs (θ_w, θ_a) in the regions (B*) and (U/B*) of diagram Fig. 8, the growing droplets do not tend to a stable filament shape. Instead the free interface undergoes a Plateau Rayleigh–like instability related to the appearance of an unstable deformation mode. A similar type of destabilizing deformation mode has been described for water filaments on a perfectly wettable stripe surrounded by a hydrophobic surface.[3] Droplets on the surface pattern undergoing the present type of instability contract into the direction of the grooves while the liquid' scenter of mass moves up, in full analogy to the instability of droplets on partially wettable stripes.[23] Like in the case of droplets on the perfectly wettable stripe the lateral contact lines remain pinned until some time after the onset of the instability. But As the lateral contact angle $\theta_\perp$ increases after the onset of the instability, at least one of the contact lines pinned on the groove ridge detaches. Owing to the interfacial energy that is stored in the metastable shape before the onset of instability, we expect to find lateral spreading by more than two grooves and, thus, irregular shape oscillations during droplet growth.

These results apply to drops covering a large number of grooves, as the stripe model implies the negligibility of finite size effects. Drops initially occupying a small number of grooves, as the ones illustrated in Sec.3, will be subjected to the same qualitative evolutions, but the location of the boundaries in the mapping of Fig.7 will specifically depend on the shape and number of wet linear features.

6 Comparison to Experiments

To validate the plane stripe model beyond the particular geometry of v–shaped grooves we performed wetting experiments on grooves with a variety of cross–sections. The plot shown in Fig. 9(a) compares the base eccentricity predicted by the chemical stripe model for an asymptotically large number of wet grooves to the experimentally measured asymptotic base eccentricities of droplets growing on a series of grooved substrates with different cross–section, c.f. Fig.2. For each groove geometry, we first determined the Wenzel angle $\theta_w(\theta_0)$ and the static advancing contact angle $\theta_a(\theta_0)$ for the given material contact angle θ_0. By virtue of the identification of angles $(\theta_w, \theta_a) = (\theta_\parallel, \theta_\perp)$ for droplets in the bidirectional growth regime we consider the numerically computed base eccentricity of the chemical stripe model $\varepsilon(\theta_\parallel, \theta_\perp)$ shown in Fig.7(b) to predict the asymptotic value of the base eccentricity ε^∞. In general, the Wenzel angle θ_w and the static advancing contact angle θ_a are expressed by

$$\theta_w = \arccos\left(r\cos\theta_0\right) \quad \text{and} \quad \theta_a = \theta_0 + \Delta\theta_a \ , \tag{12}$$

where r denotes the ratio of true to projected area of the grooved sample and $\Delta\theta_a$ the pinning interval. Corresponding expressions to compute r and $\Delta\theta_a$ for the series of groove cross–sections in Fig. 2 are summarized in table 1.

Besides a good match between the chemical stripe model and the experimental data for low contact angles, we observe that the experimentally measured base eccentricities ε of droplets growing on v–groove and rectangular grooves drop to very low values if the value the apparent contact angle $\theta_\parallel$ in side–view exceeds a certain threshold value.

For rectangular grooves, this sudden drop occurs for apparent contact angle $\theta_\parallel > \pi/2$, c.f. Fig. 9(a). This is as expected since the de–pinning angle of the rectangular groove pattern will saturate to $\theta_a = \pi$ if the material contact angle θ_0 exceeds $\pi/2$. In that case, the corresponding droplet shape on the chemical stripe is characterized by an apparent contact angle
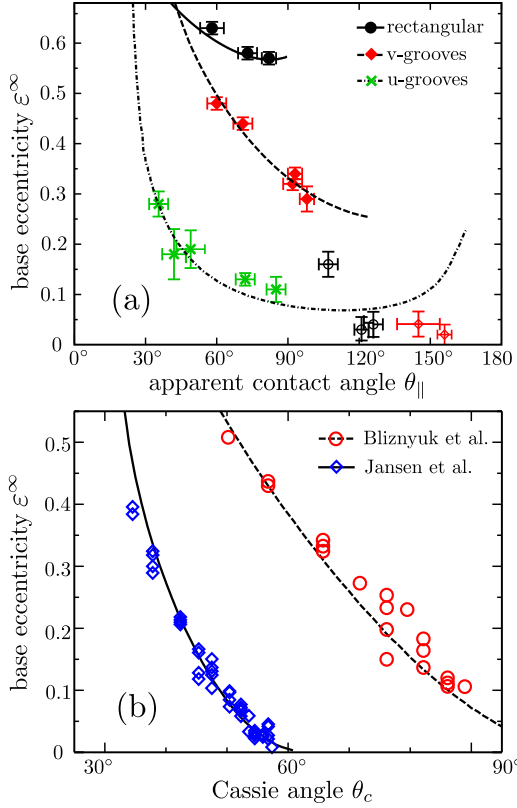
Figure 9: (a): Asymptotic base eccentricity ε^∞ of droplets in the scale-invariant regime for various groove geometries as a function of the apparent contact angle $\theta_\parallel$ in side view. Symbols indicate experimental data points, lines the numerical prediction of the plane stripe model for Wenzel state droplets, c.f. also the plot in Fig. 7(b). (b): Asymptotic base eccentricity ε^∞ according to the plane stripe model (dashed and solid lines) for a chemical pattern of alternating linear stripes in comparison to experimental data from Bliznuyuk et al.[17] with $\theta_1 = 40°$, $\theta_2 = 106°$ and Jansen et al.[18] with $\theta_1 = 31°$, $\theta_2 = 60°$.

Table 1: Wenzel roughness factor r and pinning angle $\Delta\theta_a$ for Eqns. (12) for different groove cross–sections

cross–section	r	$\Delta\theta_a$
rectangular	$1 + \frac{H^2}{BW}$	$\frac{\pi}{2}$
triangular	$\sqrt{1 + \frac{4H^2}{W^2}}$	$\arctan\left(\frac{2H}{W}\right)$
parabolic	$1 + \frac{8H^2}{3BW} - \frac{32H^4}{5B^3W}\ldots$	$\arctan\left(\frac{4H}{B}\right)$

$\theta_\perp = \theta_a = \pi$ and $\theta_\parallel = \theta_w > \pi/2$. At even higher material contact angles, droplets wetting rect-

angular grooves with flat ridges of the same width will be found in the suspended Cassie state[32] with an higher apparent contact angle $\theta_\parallel = \theta_c = \arccos(1 + \cos\theta_0)$. Substrates with v–grooves, constitute a particular case as the material contact angle $\theta_0 = \pi - \psi$ of the transition from the Wenzel to the Cassie state coincides exactly with the material contact angle where θ_a reaches the largest possible values, being π.

The chemical stripe model is not limited to liquid droplets wetting linear grooves and can also be applied to predict droplet shapes on periodic patterns of parallel chemical stripes. Figure 9 displays experimentally measured asymptotic droplet base eccentricities ε^∞ on plane substrates decorated with stripes of alternating material contact angles θ_1 and θ_2 from Refs.[17,18] Instead of the Wenzel angle θ_w, we now plot ε^∞ against the Cassie angle

$$\theta_c = \arccos\left(a_1 \cos\theta_1 + a_2 \cos\theta_2\right) , \qquad (13)$$

instead of the Wenzel angle as the apparent contact angle $\theta_\parallel$, where $a_1 + a_2 = 1$ are the area fractions of the differently wettable stripes. According to the Gibbs criterion, the advancing contact angle on the plane stripe pattern is given by $\theta_a = \max(\theta_1, \theta_2)$. Inspection of Fig. 9(b) reveal an almost perfect coincidence between the experimentally data from Refs.[17,18] and the prediction of the chemical stripe model.

7 Accuracy of chemical stripe model

A simple model for the drop eccentricity has been employed already in previous studies.[7,18] In analogy to the plane stripe model, anisotropic drop morphologies are identified by the pair of angles $\theta_\perp$ and $\theta_\parallel$, deduced from the pattern details. A further simplification is introduced assuming the drop profile to be described by circular arcs both in the parallel and orthogonal directions of the underlying pattern. By imposing the intersection of the circular arcs at the drop apex and the angles $\theta_\perp$ and $\theta_\parallel$ in contact to the substrate, a simple relation for the base eccentricity $\varepsilon^0(\theta_\parallel, \theta_\perp)$ can
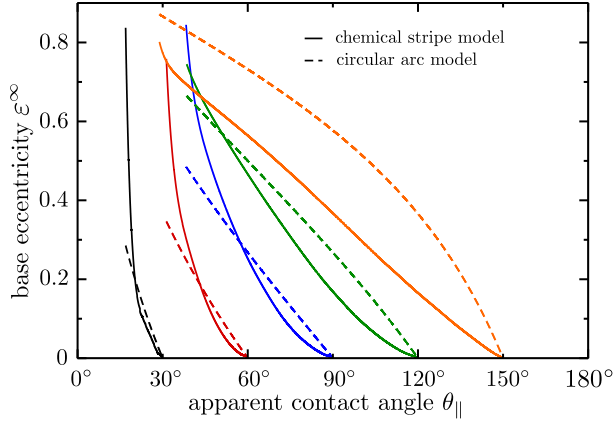
Figure 10: Comparison of droplet eccentricity ε^∞ from the wettable stripe model and the ε^0 from the circular arc model Eqn. 14. Each curve corresponds to a lateral contact angle fixed to $\theta_\perp = 30°$, $60°$, $90°$, $120°$, and $150°$ while the contact angle $\theta_\parallel$ is varied.

be deduced:

$$\varepsilon^0(\theta_\parallel, \theta_\perp) = \frac{\sin\left(\frac{\theta_\perp - \theta_\parallel}{2}\right)}{\sin\left(\frac{\theta_\perp + \theta_\parallel}{2}\right)} \ . \qquad (14)$$

Equation (14) has been compared with both numerical and experimental results[7,18] showing reasonable agreement. However the simplified model is affected by significant shortcomings: firstly Eqn. (14) does not capture the morphological bistability, and consequently is not able to discriminate between different growth modes. Secondly, it is limited to small droplet eccentricities, because strongly elongated drops clearly depart from the circular arc approximation. Furthermore, even in the limit small eccentricities, Eqn. (14) systematically overestimates the drop eccentricity, as can be seen in Fig. 10, where both models are compared. Specifically, the discrepancy quickly increases as $\theta_\parallel$ departs from the fixed value of $\theta_\perp$, with a different slope even in the limit $\theta_\parallel \to \theta_\perp$. The discrepancy becomes more pronounced as $\theta_\perp$ increases.

8 Shrinking droplets

Besides the growth regime, we employed our numerical approach to explore also the shrink-ing regime on linear pattern. An example is reported in Fig.11, for a v–groove pattern with $\psi = 15°$ and $\theta_0 = 60°$. An animation of the sequence of droplet morphologies is available in the ESI suplementary information. Starting from a droplet wetting a single groove, the volume is ramped in the usual way, until the self droplet covers 100 grooves. Then the volume is reduced, mimicking evaporation or withdrawal from a hole in the substrate. Initially the droplets shrinks longitudinally while covering the same number of grooves. Eventually the width of the liquid filament wetting the most external groove undergoes an instability and dewets the entire grow. Further volume reductions leads to progressive dewetting of more grooves while retaining an approximately circular shape. The reason for the isotropic shapes lies in the fact that the energy barriers for the lateral dewetting one groove are much lower than the barriers for wetting an additional groove, because, thanks to the absence of longitudinal pinning, the external filaments are free to shrink until a capillary instability occurs. Depending on the fluid properties small satellite droplets might be left behind the mother droplet. Only when a the number of grooves is reduced to a few units, the droplet appears elongated orthogonally, as consequence of finite size effects inhibiting the lateral instability.

9 Conclusions and Outlook

Supported by the results of both, experiments and the explicit numerical model, we propose that shapes of quasi-statically growing droplets in contact to linear grooves of arbitrary cross–section can be mapped onto corresponding equilibrium shapes of droplets confined to a plane stripe of homogeneous wettability. This mapping can be exploited to describe the shape evolution of liquid droplets that cover an asymptotically large number of grooves. The emergence of unidirectional and bidirectional growth modes can be explained from the bistability of droplets shapes on a plane chemical stripe. Various regimes of droplet growth are identi-
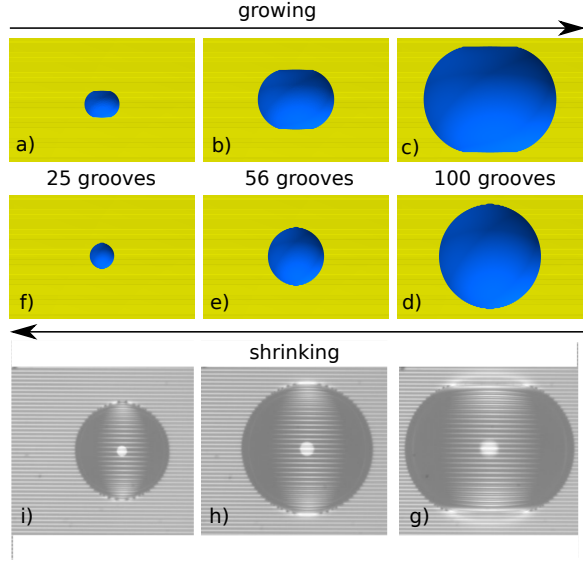
Figure 11: Snapshots of numerically computed drop morphologies during volume growth in (a) to (c) and volume loss in (d) to (f) for v–grooves with a slope angle $\psi = 15°$ and material contact angle $\theta_0 = 60°$. In each column the drop occupies the same number of grooves. Evaporating droplets observed in our experiments are shown in (g) to (i). Slope angle and material contact angle of the v–grooves are $\psi = 54.7°$ and $\theta_0 \approx 45°$.

fied and expressed in a universal diagram in terms of the Wenzel angle of the grooves and the de-pinning angle. Predictions of the chemical stripe model are validated with the experimentally measured base eccentricity of large droplets wetting grooves with either homogeneous v-shaped, rectangular, or u-shaped cross–section.

A comparison to available data from literature demonstrates that the predictions of the chemical stripe model remain valid for droplets wetting plane substrates decorated with a periodic pattern of chemical stripes of different wettability. The excellent agreement of the numerical data with the experimental results for both topographic and chemical micro–patterns underlines the universality of the chemical stripe model.

Anisotropic substrates inspired by nature, have been engineered in the recent years to speed up fog or dew harvesting.[34–36] Differences in the specific surface between localized bulge–like droplets and liquid filaments which will favor the growth of the latter droplet morphology. The mobility of the liquid will be smaller in a filament than in a localized droplet, which could potentially modify the kinetics of condensation and run–off in the presence of gravity. The comprehensive and detailed prediction provided in this work can help designing and optimising such devices.

Owing to the small width of the v–grooves being in the range of a few micrometers, we could safely excluded the influence of gravity in our experiments, even for the largest droplets considered. Flattening by gravity will break the scale–invariance of droplet shapes if the extension of their interface becomes comparable to the capillary length, being $L_g \approx 2.7mm$ for an air–water interface. On substrates with a horizontal orientation we expect that the bidirectional growth mode will be suppressed once the vertical extension of the liquid layer has surpassed a certain critical thickness being on the order of L_g.

10   Supporting Information

- Movie of a quasi-statially growing and shrinking droplet on v–grooves computed by numerical energy minimizations.

- Tabulated values of the numerically computed base eccentricity ε of a droplet on a plane chemical stripe as a function of the contact angles $\theta_\parallel$ and $\theta_\perp$.

the DAAD/MOST-Sandwich-Scholarship Programme.

References

(1) Chu, K.; Xiao, R.; Wang, E. Unidirectional liquid spreading on asymmetric nanostructured surfaces. *Nature* **2010**, *9*, 413–417.

(2) Cubaud, T.; Fermigier, M. Faceted drops on heterogeneous surfaces. *Europhys. Lett.* **2001**, *55*, 239–245.

(3) Gau, H.; Herminghaus, S.; Lenz, P.; Lipowsky, R. Liquid morphologies on structured surfaces: from microchannels to micro- chips. *Science* **1999**, *283*, 46–49.

(4) Koch, K.; Bennemann, M.; Bohn, H.; Albach, D.; Barthlott, W. Surface microstructures of daisy florets (Asteraceae) and characterization of their anisotropic wetting. *Bioinspir. Biomim.* **2013**, *8*, 036005(15).

(5) Zheng, Y.; Gao, X.; Jiang, L. Directional adhesion of superhydrophobic butterfly wings. *Soft Matter* **2007**, *3*, 178–182.

(6) Oliver, J.; Huh, C.; Mason, S. The Apparent Contact Angle of Liquids on Finely-Grooved Solid Surfaces-A SEM Study. *The Journal of Adhesion* **1977**, *8*, 223–234.

(7) Kusumaatmaja, H.; Vrancken, R.; Bastiaansen, C.; Yeomans, J. Anisotropic Drop Morphologies on Corrugated Surfaces. *Langmuir* **2008**, *24*, 7299–7308.

(8) Chung, J. Y.; Youngblood, J. P.; Stafford, C. Anisotropic wetting on tunable micro-wrinkled surfaces. *Soft Matter* **2007**, *3*, 1163–1169.

(9) Xia, D.; Brueck, S. Strongly Anisotropic Wetting on One-Dimensional Nanopatterned Surfaces. *Nano letters* **2008**, *80*, 2819–2824.

(10) Khare, K.; Zhou, J.; Yang, S. Tunable Open-Channel Microfluidics on Soft Poly(dimethylsiloxane) (PDMS) Substrates with Sinusoidal Grooves. *Langmuir* **2009**, *25*, 12794–12799.

(11) Xia., D.; He, X.; Jiang, Y.-B.; Lopez, G.; Brueck, S. Tailoring Anisotropic Wetting Properties on Submicrometer-Scale Periodic Grooved Surfaces. *Langmuir* **2010**, *260*, 2700–2706.

(12) Bliznyuk, O.; Veligura, V.; Kooij, E.; Zandvliet, H.; Poelsema, B. Metastable droplets on shallow-grooved hydrophobic surfaces. *Phys. Rev. E* **2011**, *83*, 041607(9).

(13) Fischer, G.; Bigerelle, M.; Kubiak, K.; Mathia, T.; Khatir, Z.; Anselme, K. Wetting of anisotropic sinusoidal surfaces experimental and numerical study of directional spreading. *Surf. Topogr.: Metrol. Prop.* **2014**, *2*, 044003(10).

(14) Liang, Y.; Shu, L.; Natsu, W.; He, F. Anisotropic wetting characteristics versus roughness on machined surfaces of hydrophilic and hydrophobic materials. *Applied Surface Science* **2015**, *331*, 41–49.

(15) Semprebon, C.; Mistura, G.; Orlandini, E.; Bissacco, G.; Segato, A.; Yeomans, J. Anisotropy of Water Droplets on Single Rectangular Posts. *Langmuir* **2009**, *25*, 5619–5625.

(16) Brandon, S.; Haimovich, N.; Yeger, E.; Marmur, A. Partial wetting of chemically patterned surfaces: The effect of drop size. *Journal of Colloid and Interface Science* **2003**, *263*, 237–243.

(17) Bliznyuk, O.; Vereshchagina, E.; Kooij, S. E.; Poelsema, B. Scaling of anisotropic droplet shapes on chemically stripe-patterned surfaces. *Phys. Rev. E* **2009**, *79*, 041601(6).

(18) Jansen, H.; Bliznyuk, O.; Kooij, E.; Poelsema, B.; Zandvliet, H. Simulating

Anisotropic Droplet Shapes on Chemically Striped Patterned Surfaces. *Langmuir* **2011**, *28*, 499–505.

(19) Dussan, E. On the spreading of liquids on solid surfaces: static and dynamic contact lines. *Annu. Rev. Fluid Mech.* **1979**, *11*, 371–400.

(20) Oliver, J.; Huh, C.; Mason, S. G. Resistance to Spreading of Liquids by Sharp Edges. *Journal of Colloid and Interface Science* **1977**, *59*, 568–581.

(21) Langbein, D. *Capillary Surfaces: Shape–Stability–Dynamics, in Particular Under Weightlessness*; Springer tracts in modern physics; Springer Berlin, Heidelberg, New York, 2002; Vol. 178.

(22) Tóth, T.; Ferraro, D.; Chiarello, E.; Pierno, M.; Mistura, G.; Bissacco, G.; Semprebon, C. Suspension of Water Droplets on Individual Pillars. *Langmuir* **2011**, *27*, 4742–4748.

(23) Brinkmann, M.; Lipowsky, R. Wetting morphologies on substrates with striped surface domains. *J. Appl. Phys.* **2002**, *92*, 4296–4306.

(24) Klingner, A.; Mugele, F. Electrowetting-induced morphological transitions of fluid microstructures. *J. Appl. Phys.* **2004**, *95*, 2918–2920.

(25) Dokowicz, M.; Nowicki, W. Morphology of a droplet deposited on a strip and triangular groove. *Surface Innovations* **2014**, *2*, 228–234.

(26) Snoeijer, J. H.; Andreotti, B. Moving Contact Lines: Scales, Regimes, and Dynamical Transitions. *Annual Review of Fluid Mechanics* **2013**, *45*, 269–292.

(27) Brakke, K. The Surface Evolver. *Experimental Mathematics* **1992**, *2*, 141–165.

(28) Brakke, K. The Surface Evolver and the stability of liquid surfaces. *Phil. Trans. Royal Soc. London, Ser. A* **1996**, *354*, 2143–2157.

(29) Semprebon, C.; Herminghaus, S.; Brinkmann, M. Advancing modes on regularly patterned substrates. *Soft Matter* **2012**, *8*, 6301–6309.

(30) Semprebon, C.; Forsberg, P.; Priest, C.; Brinkmann, M. Pinning and wicking in regular pillar arrays. *Soft matter* **2014**, *100*, 5739–5748.

(31) Shuttleworth, R.; Bailey, G. The spreading of a liquid over a rough solid. *Disc. Faraday Soc.* **1948**, *3*, 16.

(32) Butt, H.-J.; Semprebon, C.; Papadopoulos, P.; Vollmer, D.; Brinkmann, M.; Ciccotti, M. Design principles for superamphiphobic surfaces. *Soft Matter* **2013**, *9*, 418–428.

(33) Ferraro, D.; Semprebon, C.; T. Tóth, E. L.; Pierno, M.; Mistura, G. P.; Brinkmann, M. Morphological Transitions of Droplets Wetting Rectangular Domains. *Langmuir* **2012**, *28*, 13919–13923.

(34) White, B.; Sarkar, A.; Kietzig, A. M. Fog-harvesting inspired by the Stenocara beetle - An analysis of drop collection and removal from biomimetic samples with wetting contrast. *Applied Surface Science* **2013**, *284*, 826–836.

(35) Park, K. C.; Chhatre, S. S.; Srinivasan, S.; Cohen, R. E.; McKinley, G. H. Optimal design of permeable fiber network structures for fog harvesting. *Langmuir* **2013**, *29*, 13269–13277.

(36) Faustini, M.; Cattoni, A.; Peron, J.; Boissière, C.; Ebrard, P.; Malchère, A.; Steyer, P.; Grosso, D. Dynamic Shaping of Femtoliter Dew Droplets. *ACS Nano* **2018**, *12*, 3243–3252.

Graphical TOC Entry